JOURNAL OF MATERIALS SCIENCE 32 (1997) 2485–2499

Oxidation of TiAl based intermetallics

S. A. KEKARE*, P. B. ASWATH
Materials Science and Engineering Program and Mechanical and Aerospace Engineering Department, University of Texas at Arlington, Arlington TX 76019 USA

The high temperature oxidation behaviour of the binary and ternary alloys of the Ti–48Al system was studied at different temperatures. The primary objectives of this work were the establishment of the activation energies, the migration tendencies of the alloy species, mechanism of oxidation and chemistry of the oxide scales. The ternary additions were Cr (1.5 at %), V (2.2 at %), W (0.2 at %) and Mn (1.4 at %). The addition of ternary additions did not play a significant role in the oxidation behaviour at 704 °C. At 815 °C the alloys with Cr and V exhibited linear oxidation behaviour with large weight gains while the base Ti–48Al alloys exhibited the best behaviour. At 982 °C the Mn-containing alloy was the worst, exhibiting a linear oxidation behaviour while the alloy with V and W and the base alloy with 400 p.p.m. oxygen exhibited the best oxidation behaviour. At 982 °C the outermost oxide layer in contact with air is always near stoichiometric TiO_2. In all the alloys a layer of porosity is created just below the outer TiO_2 layer by the Kirkendall mechanism due to the rapid outward diffusion of Ti atoms. The addition of trivalent atoms like Cr in small amounts appear to be detrimental to the oxidation process as they can generate additional oxygen vacancies while the addition of atoms with valence of 5, such as V, and 6, such as W, appear to have beneficial effect on the oxidation behaviour at 982 °C by tying up oxygen vacancies.

1. Introduction

Titanium aluminide-based intermetallics are of interest for applications that require high specific strength at elevated temperatures like hypersonic aircraft, gas turbines etc. The problems of low ductility and toughness have been partly alleviated by changing the chemistry and microstructure of the alloys. The current state of research indicates that the binary alloys with the best combination of strength and toughness are centred around the composition Ti–48Al (at%) [1]. Ternary additions of Cr, V and Mn appeared to increase the ductility of the two phase Ti–48Al base alloys [2, 3]. However, before these materials are used at elevated temperatures a comprehensive understanding of their behaviour under high temperature oxidation environments needs to be developed.

Oxidation of any metal proceeds by two processes, oxygen dissolution and oxide scale formation. Typically the formation of an oxide scale of finite thickness on the metal surface indicates that oxygen dissolution proceeds at a lower rate compared to oxidation. The total oxidation rate is therefore governed by the diffusion of the active elements required for oxidation through the oxide scale. Prominent factors that affect the transport characteristics of the scale are concentration of the diffusing species and existence of high diffusivity paths like cracks, pores and grain boundaries within the oxide [4]. Hence, conditions that alter these factors are responsible for changes in the oxidation response of the base alloy.

The initial oxides may grow as whiskers normal to the metal surface or as a laterally spreading film. The whiskers, after growing a certain distance normal to the surface, turn sideways to connect with other whiskers and form a film. This mechanism leaves a large amount of porosity under the film generated by joining of the whiskers [5]. Once the whole metal surface is covered by the oxide film, elemental activity at the oxide–metal interface dictates further oxidation. Depending on the oxygen pressure and metal activity, either Ti or Al may oxidize preferentially. The initial oxidation is brought about by diffusion of metal to the surface but, after formation of the oxide films, the oxidation proceeds by diffusion of oxygen through the initial layers towards the metal. This predicts the parabolic nature of the oxidation response. The diffusivity of Ti in rutile is faster than that of oxygen, whereas Al diffuses at a very slow rate in alumina. This results in an outward growth of rutile and an inward growth of alumina [5]. Thus, channels of rutile and alumina are seen, side by side, in the intermediate mixed oxide layer. The only difference between them is that alumina progresses towards metal–oxide interface and rutile grows towards the gas–oxide interface.

The presence of a ternary element can alter the activities of the Ti and Al and thus change the thermodynamics of the oxidation process. Ternary elements can also change the concentration of the active diffusing species and hence the kinetics of the oxidation

* *Present address*: Rockwell Semi Conductor Systems, Newport Beach, CA 92660 USA.

0022–2461

process. In addition the presence of ternary elements can change the lattice parameters of the oxide and the alloy thus affecting the characteristics of the oxide/alloy interface. In this study the role played by the ternary elements Cr, V, W and Mn on the oxidation process are studied.

Details of the experimental procedure are given in Section 2, the thermodynamic, kinetic and physical models of oxidation are detailed in Section 3. Section 4 details the experimental results and discussion and Section 5 lists some of the key conclusions.

2. Experimental procedure

The alloys studied were provided by McDonnell Douglas Research Laboratories in the form of extruded rods. Table I lists all the alloy compositions. Test samples were cut from the rods, normal to the extrusion direction. The samples were polished and ultrasonically cleaned in acetone and their dimensions measured to an accuracy of 0.01 cm. Average dimensions of the samples were 5 mm square with 1 mm thickness. The samples were oxidized in a Perkin-Elmer 7-series integrated thermal analysis system. Continuous weight gain data were recorded and data analysis was performed with a 7700 series computer used in conjunction with the thermal analysis system. A flow of 172.5 kPa compressed air ($50\,cm^3\,min^{-1}$) was introduced into the furnace when the test temperature was reached and was maintained constant throughout the duration of the test. The alloys were tested at temperatures of 704, 815 and 982 °C. The oxidation data were represented as weight gain per unit area of exposed specimen versus time to identify the type of oxidation. The oxidation rate constants were then calculated from the oxidation data.

The oxidized samples were mounted and sectioned to obtain a profile of the oxide scale. These profiles were studied under a Cambridge Instruments (Stereoscan 120) scanning electron microscope and a CAMICA (CAMIBAX) electron probe micro analyser. The scanning electron microscopy observations were aimed at the surface topography of the outer layers and the integrity of the overall scale. The microprobe studies investigated the migration tendencies of the elements throughout the scale and also the composition of individual layers. A scanning X-ray dot mapping technique using wavelength dispersive spectroscopy (WDS) was used to study the elemental distribution within the oxide layers. Quantitative elemental analysis was obtained by stepping the electron beam in a straight line across the oxide layers and the base metal and known material standards were used for data reduction.

In addition, after oxidation at 982 °C for 6000 min in air, the oxide scale on the binary Ti–48 at %Al alloy was scraped off and powdered. As the amount of oxide formed was insufficient for powder X-ray diffraction, samples were mounted on and examined in the transmission electron microscope. Selected area diffraction patterns were taken to confirm the structure of oxide.

TABLE I Composition of the alloys

Alloy stoichiometry
Ti–48Al (600 p.p.m. oxygen)
Ti–48Al (400 p.p.m. oxygen)
Ti–48Al–1.5Cr (at %)
Ti–48Al–2.2V (at %)
Ti–48Al–1.4Mn (at %)
Ti–48Al– 0.2W (at %)

3. Models for oxidation of TiAl based intermetallics

In modelling a complex process like oxidation, several factors can interact in a synergistic fashion and control the oxidation process. The oxidation process in itself is a chemical reaction and all the laws of physical chemistry are applicable. The formation and stability of the reaction products depend on the thermodynamic conditions of the alloy system, temperature and the environment. The kinetics of the oxidation process is a function of the type of oxidation product formed as well as its structural integrity. In addition the defect structure of the corrosion product determines the rate of diffusion of the active species. In this section, an effort is made to model the high temperature oxidation of titanium aluminides by considering all possible aspects of oxidations.

3.1. Thermodynamics of the oxidation of TiAl

A basic understanding of the oxidation process is developed by studying the thermodynamics of the oxide formation of the two primary elements Ti and Al. In this model the effect of activities of the constituent elements and the partial pressure of oxygen are examined. As there is little miscibility between Ti oxides and Al oxides the analysis considers the formation of pure oxides.

It is possible to calculate the oxygen equilibrium pressure of a metal/oxide system from the free energy of formation of the oxide, e.g.

$$2Al + \tfrac{3}{2}O_2 = Al_2O_3 \quad (1)$$

the free energy change ΔG_1^0 in this reaction is given by

$$\Delta G_1^0 = -RT\ln K_1 \quad (2)$$

where

$$K_1 = \frac{a_{Al_2O_3}}{a_{Al}^2 P_{O_2}^{3/2}} \quad (3)$$

In order to form a pure oxide from a pure metal, the activities of pure elements and oxides are given by $a_{Al} = a_{Al_2O_3} = 1$ then the partial pressure of oxygen P_{O_2} (Al/Al_2O_3) for this reaction is given by,

$$\ln P_{O_2}(Al/Al_2O_3) = \frac{2\Delta G_1^0}{3RT} \quad (4)$$

In a similar fashion, the Ti/TiO_2 equilibrium can be represented as

$$Ti + O_2 = TiO_2 \quad (5)$$

and the equilibrium constant for this reaction can be expressed by

$$K_2 = \frac{a_{TiO_2}}{a_{Ti} P_{O_2}} \quad (6)$$

Similarly, for the formation of pure oxide from pure metal, if the activities of the pure metal and oxide are unity then

$$\ln P_{O_2}(Ti/TiO_2) = \frac{\Delta G_2^0}{RT} \quad (7)$$

where ΔG_2^0 is the change in free energy due to reaction 5 (Equation 5). In a pure metal/gas system, where the activities of the metal and the oxide are unity, the direction of the reaction solely depends upon the oxygen pressure. The equilibrium pressures can also be calculated for binary and ternary alloy systems, if the activities of elements in the alloy at the temperature of oxidation are known. For oxidation of Ti and Al, one can assume that the oxides are in pure form i.e. $a_{TiO_2} = a_{Al_2O_3} = 1$ but the activity of Ti in the oxides within the oxides or the base metal is not unity ($a_{Ti} \neq 1$). It can be shown from first principles that Equations 4 and 7 can be written as Equations 8 and 9, respectively, [6]

$$\ln P_{O_2}(Al/Al_2O_3) = \tfrac{2}{3} \ln K_1 - \tfrac{4}{3} \ln a_{Al} \quad (8)$$

$$\ln P_{O_2}(Ti/TiO_2) = \ln K_2 - \ln a_{Ti} \quad (9)$$

When pure elemental oxidation is considered, the free energy of formation of alumina is more negative compared to that of rutile, at all temperatures [7]. Hence if a mixture of TiO_2 and Al_2O_3 were considered, TiO_2 should be reduced to TiO by Al if the activities of the pure elements and oxides were unity. (TiO_2 is not reduced to Ti because Ti/TiO and Al/Al_2O_3 equilibrium exhibit similar oxygen pressure dependence [6]). In addition, it is well established that Ti can oxidize to various valence states like Ti^{2+}, Ti^{3+} and Ti^{4+} yielding metastable oxides TiO and Ti_2O_3 and the stable oxide TiO_2 [8]. These metastable oxides have equilibrium pressures very close to that of Al_2O_3 and slight changes in activities of the constituent elements can bring about a radical change in the type of the oxidation product.

Rahmel and Spencer have performed an extensive analysis of the thermodynamics of the Ti–Al–O system [6]. According to their analysis, the equilibrium partial pressures of oxygen for Al/Al_2O_3 equilibrium and for Ti/TiO equilibrium are approximately the same in the single phase γ-TiAl composition range at 900 °C and in two phase $Ti_3Al + TiAl$ composition range. The preferred oxide will be TiO rather than Al_2O_3. They calculated the partial pressures of oxygen in the single phase Ti_3Al region and demonstrated that the partial pressure of oxygen for the formation of Al_2O_3 is higher than that required for the formation of TiO, thus stabilizing the TiO over Al_2O_3. As Ti continues to oxidize, the metal near the oxide scale gets locally enriched in Al, thereby entering into the $TiAl + TiAl_3$ composition range. In this composition range, the partial pressure of oxygen for the formation of TiO is 3–4 orders of magnitude greater than that required for the formation of Al_2O_3. This results in termination of oxidation of Ti and initiation of Al_2O_3 formation. Thus for a particular oxide to form, it is not only necessary that the element be present at the metal–gas or oxide–metal interface, but also that the partial pressure of oxygen exceeds the equilibrium pressure for the reaction at that activity of the element. The overall oxidation proceeds in this manner to generate an oxide scale consisting of alternating layers of Ti and Al oxides.

The oxide formed at the air–oxide scale interface is typically TiO_2 as the partial pressure of oxygen is highest at that site. As we move away from the oxide–gas interface towards the oxide–metal interface, the oxides of Ti would have a decreasing order of valence of the Ti atom (+ 4 to + 2) due to a decrease in the oxygen partial pressure. Al has only one form of oxide throughout the different layers in the scale. The only difference seen in the Al_2O_3 oxide within the different layers is in the morphology of the film as the partial pressure of oxygen goes on decreasing. Aluminium, typically has a Pilling–Bedworth ratio greater than one. This indicates the existence of residual compressive stresses in the Al_2O_3 film [9]. Nearer the metal surface, the oxide is subjected to constraints from both the metal below and the outer oxide layers. This results in cracking and delamination of the oxide layer from the metal surface.

3.2. Kinetics of the oxidation of TiAl

The kinetics at the initiation of oxidation are controlled by the availability of oxidation sites while the kinetics during the steady state oxidation is controlled by the rate of diffusion of the diffusing species through the oxide scale. The model detailed below assumes a compact oxide layer with minimum defects and the rate controlling steps in the oxidation are the diffusion of the active species through the oxide scale.

It is generally accepted that TiO_2 is a *n*-type semiconductor [10]. Kofstad concluded, based on studies of non-stoichiometric TiO_2, that the interstitials based on Ti^{3+} as well as Ti^{4+} exist along with doubly ionized oxygen vacancies [10]. Marker experiments indicate that in addition to diffusion of Ti in TiO_2, inward diffusion of oxygen also plays an important role in the oxidation process [11, 12]. Thus, it can be concluded that in addition to Ti vacancies oxygen vacancies are a mobile species in the oxide layer and the doubly ionized oxygen vacancies have a significant role in the oxidation of TiAl. The formation of these vacancies can be explained by using the Kroger–Vink notation. This notation uses the following symbols to indicate the reactant and product species: M_M = Metal ion at metal site in the oxide lattice; O_O = Oxygen ion at oxygen site in the oxide lattice; V_M = Neutral vacancy in the metal site in the oxide

lattice; V_O = Neutral vacancy in the oxygen site in the oxide lattice; N_M = N ion at the metal site in the oxide lattice.

If a vacant site carries a charge with respect to the perfect oxide lattice, it is represented by a superscript on the vacancy subscript. For a vacant site which is negative with respect to the lattice, the subscript carries a vertical dash and for a positive vacant site, the subscript carries a dot. The number of dots or dashes corresponds to the number of free electrons or holes created. For example, a vacant oxygen site which has lost one electron carries a $+1$ charge and is indicated by the symbol $V_{\ddot{O}}$. The formation of the doubly ionized oxygen vacancies can be represented by

$$\begin{aligned} O_O &\Leftrightarrow V_{\ddot{O}} + \tfrac{1}{2}O_2 + 2e' \\ K_3 &= P_{O_2}^{1/2}[V_{\ddot{O}}]n^2 \end{aligned} \tag{10}$$

where O_O is an oxygen anion with the usual charge and $V_{\ddot{O}}$ is a doubly ionized oxygen vacancy from which both the electrons are freed, n is the concentration of electrons that are freed from oxygen vacancies and K_3 is the equilibrium constant for this reaction. The conditions of electrical neutrality require that the positive and negative charges be balanced i.e. $2V_{\ddot{O}} = n$. In this case, vacancy concentration is shown to be

$$[V_{\ddot{O}}] = \frac{K_3^{1/2} P_{O_2}^{-1/6}}{4^{1/3}} \tag{11}$$

The oxygen ion vacancy concentration depends on the temperature and the oxygen partial pressure. Depending on the type of defect formed the following general relationship of the defect concentration in TiO_2 can be stated

$$C_{\text{defect}}(TiO_2)\,\alpha\, P_{O_2}^{-1/n}$$

From the discussion of the steps in oxidation of Ti–48Al alloys, it can be inferred that if the growth of TiO_2 becomes restricted then it is possible to slow down the overall process of oxidation of these alloys. As mentioned earlier, the doubly ionized oxygen vacancies are the rate controlling species during the growth of TiO_2 over Ti. In addition Al_2O_3 forms below the outer TiO_2 layer. Hence the oxygen necessary for Al_2O_3 formation must diffuse through the TiO_2. Any dopant in the TiO_2 crystal, which is able to reduce the concentration of these vacancies will, in effect, retard the oxidation of these alloys. For example the addition of tungsten can potentially form WO_3 with a cation of valence $+6$ which can dissolve in TiO_2 and annihilate the oxygen vacancies by the following reactions

$$WO_3 + V_{\ddot{O}} \Leftrightarrow W_{\ddot{T}i} + 3O_O \tag{12}$$

$W_{\ddot{T}i}$ is the W^{6+} ion occupying a normal Ti^{4+} site and carries a $+2$ charge with respect to the lattice. Then the electroneutrality is satisfied by

$$2[V_{\ddot{O}}] + [W_{\ddot{T}i}] = n \tag{13}$$

when $[W_{\ddot{T}i}] \gg [V_{\ddot{O}}]$, $[W_{\ddot{T}i}] = n$, and K_4 is the equilibrium constant of reaction 13, the concentration of vacancies is given by

$$[V_{\ddot{O}}] = \frac{K_4}{[W_{\ddot{T}i}]^2} P_{O_2}^{-1/2} \tag{14}$$

However, if the ternary species does not dissolve in the oxide at all or if the concentration of dopant ions in the oxide scale is very low compared to that of the oxygen vacancies $[V_{\ddot{O}}] \gg [W_{\ddot{T}i}]$ then $2[V_{\ddot{O}}] = n$ and the equilibrium vacancy concentration is given by Equation 11. Thus it can be seen that the ternary elements are beneficial in increasing resistance to oxygen diffusion only if they oxidize along with Ti and migrate to the TiO_2 layer in concentrations larger than that of the oxygen vacancies.

This analysis can be applied to any ternary alloy addition and methods to calculate the amount of addition for obtaining optimum effects have been derived [13]. This analysis also shows the detrimental effect of addition of ternaries which form cations with valence less than $+4$. For example, Cr dissolved in TiO_2 layer will accelerate the oxidation by formation of doubly ionized oxygen vacancies by the reaction given below

$$Cr_2O_3 \Leftrightarrow 2Cr_{Ti} + 3O_O + V_{\ddot{O}} \tag{15}$$

This increase in the population of the mobile defects can lead to an increased rate of oxidation.

Other models have been used to explain the mechanism of oxidation. For example smaller atomic radii elements like Cr, Mn and V are believed to cause a reduction in the diffusivity of oxygen by acting as a trap for oxygen [14].

An element which is beneficial for oxidation resistance according to the kinetics aspect of the analysis may prove to be disastrous if it leads to the stabilization of transient oxides which are not structurally stable. In particular, if an element promotes a slow growth of the scale, it can potentially give rise to non-equilibrium oxides like TiO and Ti_2O_3 by not allowing sufficient oxygen to diffuse through the scale. These oxides are typically powdery and cause delamination of scale at the oxide scale–metal interface.

The analysis provided above assumes a monolithic layered scale of oxides, which favors bulk diffusion. This is rarely encountered in real life situations and almost always the oxidation advances by diffusion of species along high diffusivity paths such as grain boundaries, porosity and cracks. The effect of these defects in the scale needs to be adequately accommodated in the analysis. In addition in this analysis, the only diffusion barrier for the movement of oxidizing species is its own oxide. In the case of binary alloys such as TiAl, a further resistance to Ti diffusion is offered by the intermediate Al_2O_3 layers.

3.3. A physical model for oxidation of TiAl base alloys

Fig. 1 represents a schematic of the proposed mechanism of oxidation behaviour of TiAl intermetallics.

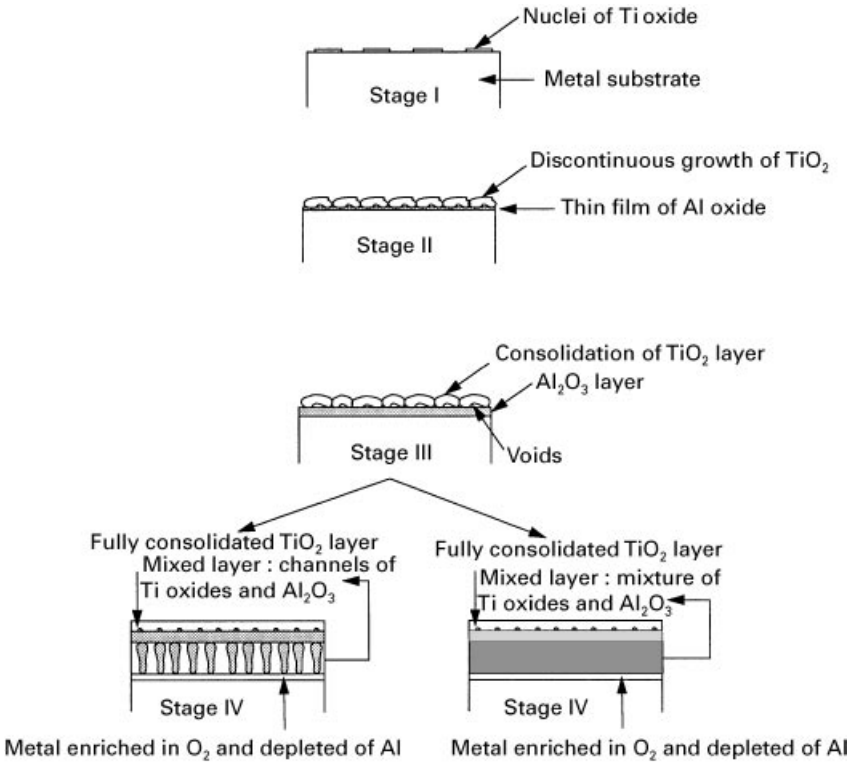

Figure 1 A physical model detailing the different stages of oxidation in binary and ternary TiAl based intermetallic alloys.

This model is similar to the one postulated by Taniguchi *et al.* [5] for oxidation in a pure oxygen environment, with some salient differences outlined below. In the early stages of oxidation, (stage I and stage II) isolated islands of oxide are formed. Titanium oxide crystals in these islands grow, both vertically and horizontally, consuming Ti from the surroundings. The kinetics of Ti oxide formation are typically greater than that of Al_2O_3 formation. Consequently, the metal surface is rapidly covered with a thin layer of Ti oxide. This leads to a local enrichment of the intermetallic in Al below the oxide surface locally changing the stoichiometry which favours the formation of Al_2O_3. The diffusion of Ti appears to follow a Kirkendall mechanism for interdiffusion. As the outward diffusion of Ti is very rapid, it leaves behind a small amount of porosity at the Ti oxide/Al_2O_3 interface. We believe that as a continuous outer oxide scale of Ti oxide is formed, its exposure to air in the absence of Al will convert all the transient Ti oxides, such as TiO, Ti_2O_3 and Ti_3O_5, to pure TiO_2. Once the outer layer of TiO_2 and the inner layer of Al_2O_3 are sufficiently thick, the oxidation proceeds by diffusion of oxygen into the scale and outward diffusion of Ti ions. This leads to two possibilities. The first is the formation of alternate channels of TiO_2 and a mixture of Al_2O_3 and TiO_2 oxides. The other possibility is the formation of a mixture of TiO_2 and Al_2O_3 in the interior, as shown in stage IV. Simultaneously it can be seen that a depletion layer of Al (enriched with Ti) is formed at the oxide–metal interface, due to outward diffusion of Al from the alloy into the intermediate layer. Below this is a small region which can be called an oxygen affected zone which is embrittled and can potentially develop cracks.

The morphology of the oxides in the interior is a function of the ratio of diffusion coefficient of the oxidizing species in the intermetallic and the oxide scale. If this ratio is larger than unity then the species arrives at the metal–oxide interface faster than it gets oxidized and the metal–oxide interface is planar. On the other hand, if the ratio is less than unity then the oxidation takes place faster at sites where the oxide surface is nearest to the metal. This results in extension of the oxidized zone further into the metal, resulting in a spiked metal–oxide interface.

4. Results and discussion

Results obtained from isothermal oxidation tests at 704, 815 and 982 °C for durations of 6000 min each are discussed. The most common way of representing the results of oxidation is plotting the weight gained by the material for unit area as a function of time of oxidation. The data from these analyses usually fit one of several laws governing the rate equations which include linear growth law, parabolic growth law and logarithmic growth law and in some cases a combination of these. In addition, some other growth laws like inverse logarithmic and inverse parabolic laws have been postulated. A drawback to using these laws over the whole range of the test is that one may fail to notice some of the nuances of the oxidation response. The first step in our analysis involved a reduction of the data and plotting it in terms of weight gain versus time. Secondly the favoured macroscopic oxidation

TABLE II Mechanism of oxidation at different temperatures

Alloy stoichiometry	704 °C	815 °C	982 °C
Ti–48Al (600 p.p.m. oxygen)	Parabolic	Parabolic	Parabolic
Ti–48Al (400 p.p.m. oxygen)	Parabolic	Parabolic	Parabolic
Ti–48Al–1.5Cr (at %)	Parabolic	Linear	Parabolic
Ti–48Al–2.2V (at %)	Parabolic	Linear	Parabolic
Ti–48Al–1.4Mn (at %)	Parabolic	Parabolic	Linear
Ti–48Al–0.2W (at %)	Parabolic	Parabolic	Parabolic

growth law was identified. In our tests, only two oxidation rate laws were applicable: parabolic law given by $W^2 = K_p t$ or linear growth law given by $W = K_p t$ where W = weight gain in $mg\,cm^{-2}$ and t = time in minutes and K_p = oxidation rate constants with units of $mg^2\,cm^{-4}\,min^{-1}$ in parabolic oxidation and units of $mg\,cm^{-2}\,min^{-1}$ in linear oxidation. Table II lists the mechanism of oxide growth in each of the alloys at the three different temperatures, in air and in oxygen.

4.1. Oxidation at 704 °C

All the binary and ternary alloys exhibited parabolic oxidation behaviour when oxidized in air at this temperature. The total weight gain/unit area is very limited in all the alloys and was within the sensitivity range of the balance in the thermogravimetric setup. This resulted in several small spikes which correspond to random fluctuations in the balance readings (note: As the sample was placed in a Pt pan, there is theoretically no possibility of weight decrease). Fig. 2 is the weight gain plotted as a function of time for all the alloys. Even in the worst case the total weight gain is below 0.35 $mg\,cm^{-2}$ after 6000 min of exposure and in the best case the total weight gain is 0.1 $mg\,cm^{-2}$ after 6000 min. The oxidation rate constant varies between 4×10^{-6} to $2.5 \times 10^{-5}\,mg^2\,cm^{-4}\,min^{-1}$ for all the alloys as shown in Fig. 3. There is a transient oxidation state followed by a region of steady state oxidation behaviour. The initial transient which exhibits a fairly large oxidation rate corresponds to the point where there is no protective oxide scale present to retard the oxidation process. A stable oxide scale that covers the complete surface is formed after about 1000 min at this temperature. Once a stable oxide scale is formed all subsequent oxidation is controlled by the rate of diffusion of oxygen ions through the oxide scale to the oxide metal interface to continue the oxidation process. At this point a true parabolic oxidation behaviour is observed with a nearly constant rate constant which conforms to the parabolic growth law. The amount of oxide scale formed on the surface was very small and no attempt was made to perform quantitative electron probe microanalysis. The data indicates that, at this temperature, there is not much of a variation in the oxidation response of all the alloys. The ternary alloy with W shows the highest oxidation rate constant while the rest of the alloys are similar in their oxidation behaviour. For calculation of activation energy the weight gain versus time curve was smoothed with a curve fit and the slope determined.

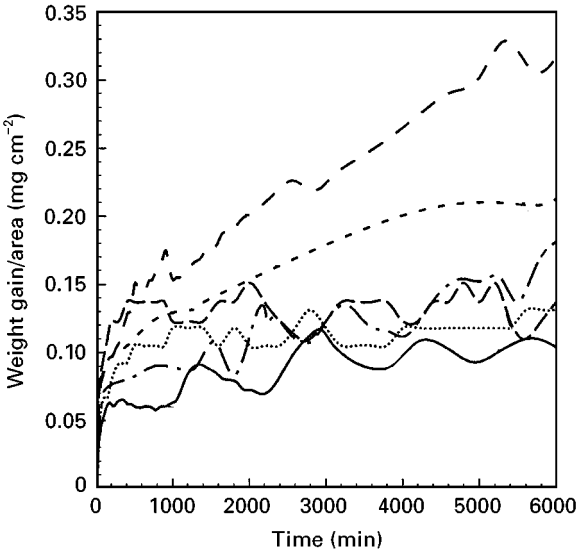

Figure 2 Weight gained per unit area as a function of time for all the alloys oxidized at 704 °C in air. Ti–48Al plus 0.2W (– – –), 2.2V (- - -), 1.5Cr (·–·), 400 p.p.m. O_2 (···), 600 p.p.m. O_2 (– – –), 1.4Mn (——).

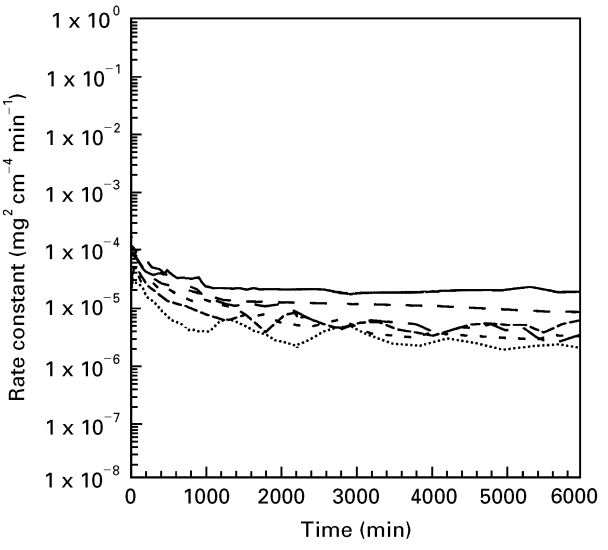

Figure 3 Oxidation rate constant as a function of time for all the alloys oxidized at 704 °C in air. Ti–48Al plus 0.2W (——), 2.2V (— —), 400 p.p.m. O_2 (– – –), 600 p.p.m. O_2 (— — —), 1.5Cr (- - -), 1.4 Mn (···).

4.2. Oxidation at 815 °C

All the alloys exhibit parabolic oxidation with the exception of two ternary alloys with V and Cr which exhibit linear oxidation behaviour when oxidized in air at 815 °C. The binary alloys and the ternary alloys with W and Mn, exhibit oxidation behaviour which is very similar as seen in the weight gain plots shown in Fig. 4, with a total weight gain in the range of 1–2 $mg\,cm^{-2}$ after 6000 min. However, the ternary alloys with Cr and V show significantly larger weight gains of the order of 7–10 $mg\,cm^{-2}$ after 6000 min coupled with a linear oxidation response. The oxidation rate constants for the alloys are shown in Fig. 5(a) and (b). In the binary alloys and the alloys with W and Mn the rate constants vary between 2.5×10^{-4} and

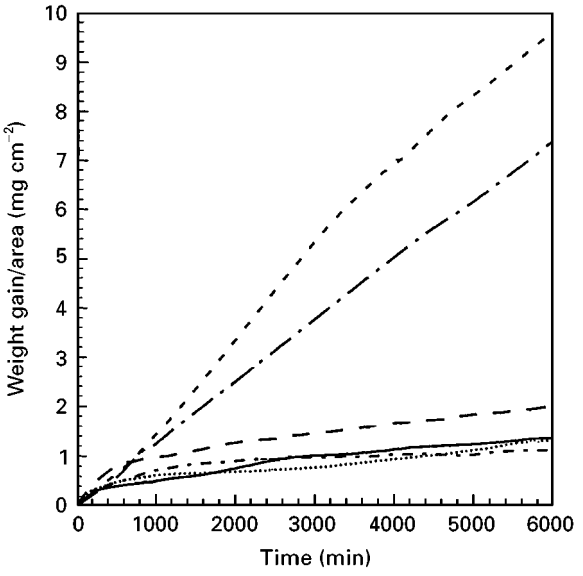

Figure 4 Weight gained per unit area as a function of time for all the alloys oxidized at 815 °C in air. Ti–48Al plus 2.2V (- - -), 1.5Cr (—·—), 0.2W (—·—), 1.4Mn (—), 400 p.p.m. O_2 (··), 600 p.p.m. O_2 (— - —).

9×10^{-4} mg^2 cm^{-4} min^{-1}. At 815 °C there is a region of transient oxidation followed by a near parabolic oxidation response in these alloys as shown in Fig. 5(b). The transient region is of the order of 200–500 min, depending on the alloy. This is possibly because a protective oxide layer is formed quicker at 815 compared to 704 °C. After the initial transient region both the binary alloys with 400 and 600 p.p.m. of internal oxygen show a gradual drop in the value of the oxidation rate constant. However, the binary alloy with 400 p.p.m. of oxygen exhibited a sharp increase in oxidation rate at around 3000 min. This can be attributed to the formation of cracks in the oxide scale which allow for the penetration of oxygen more easily to the oxide–alloy interface. Analysis after oxidation indicated the presence of several cracks in the alloy with 400 p.p.m. oxygen while the alloy with 600 p.p.m. of oxygen was relatively compact. The two ternary alloys with Cr and V exhibited linear oxidation rates between 0.002 to 0.004 mg cm^{-2} min^{-1} as shown in Fig. 5(b). The alloy with Cr shows limited transient oxidation behaviour in the first 400 min. The cross-section of this oxide scale showed extensive cracks that penetrated all the way from the oxide–gas interface to the oxide–alloy interface promoting easy pathways for oxygen diffusion. The ternary alloy with V also shows a transient behaviour followed by a gradual decrease in the oxidation rate. However, the alloy with V is much worse than the alloy with Cr at 815 °C. Overall at 815 °C the addition of Mn and W do not appear to cause any changes in the oxidation behaviour compared to the binary alloy while the addition of Cr and V is detrimental to the rates of oxidation.

4.3. Oxidation at 982 °C

Oxidation tests were performed for all the alloys in an environment of air at 982 °C. At 982 °C substantial oxide scale was formed on the surface facilitating

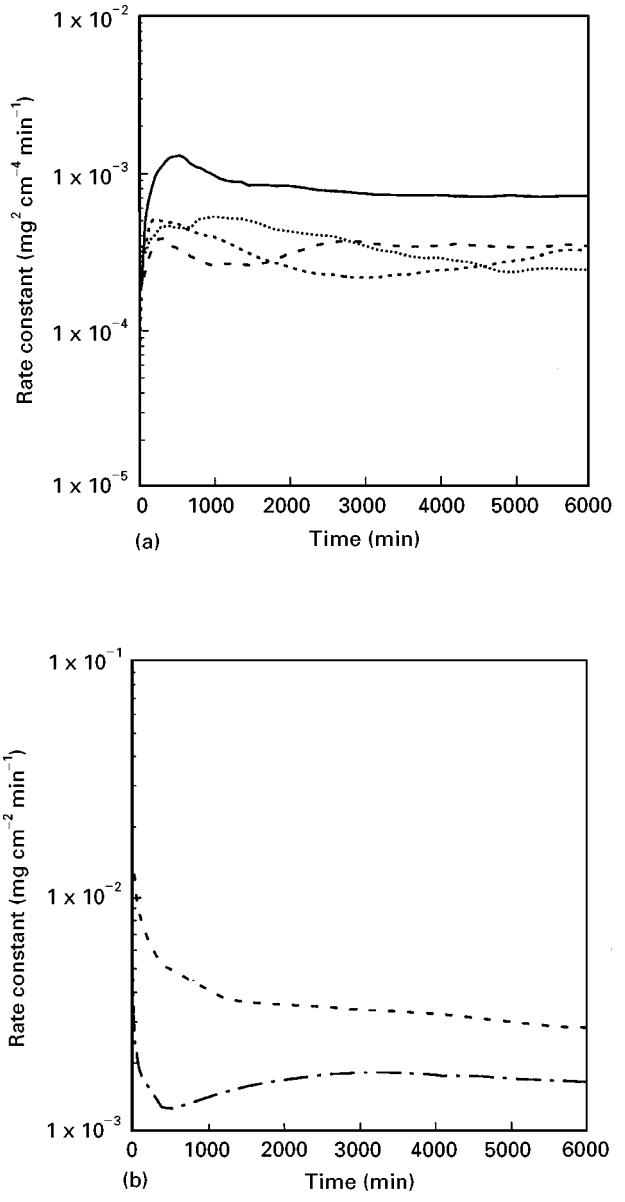

Figure 5 (a) Parabolic oxidation rate constant as a function of time for the binary alloys and the alloys with Mn and W oxidized at 815 °C in air. (b) Linear oxidation rate constant as a function of time for the ternary alloys with V and Cr oxidized at 815 °C in air. Ti–48Al plus 0.2W (———), 1.4Mn (— — —), 600 p.p.m. O_2 (···), 400 p.p.m. O_2 (- - -), 2.2V (– – –), 1.5Cr (— - —).

a complete analysis of the oxide scale morphology using qualitative and quantitative electron probe microanalysis. Due to the detailed results for each alloy, after a general discussion of the kinetic aspects of the oxidation of all the alloys a more detailed analysis of the oxidation behaviour of each of the alloys is attempted.

All the alloys exhibit a parabolic oxidation behaviour with the exception of the ternary alloy with Mn which exhibits a linear oxidation behaviour at 982 °C. Fig. 6 is a plot of the weight gained per unit area as a function of time due to oxidation in an environment of air for all the alloys. The total weight gained after 6000 min of oxidation varies between 20–60 mg cm^{-2} for the alloys, the ternary alloy with V being the best and the ternary alloys with Mn and Cr being the worst. Fig. 7(a) shows all the parabolic oxidation rate

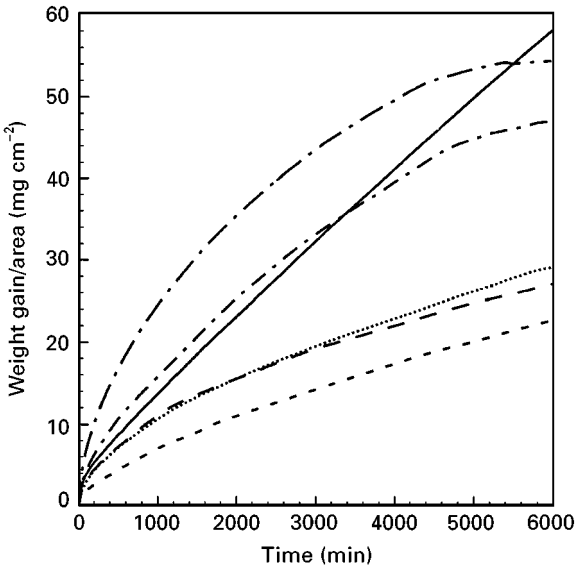

Figure 6 Weight gained per unit area as a function of time for all the alloys oxidized at 982 °C in air. Ti–48Al plus 1.5 Cr (—·—), 600 p.p.m. O_2 (—·—), 1.4 Mn (—), 0.2 W (– – –), 400 p.p.m. O_2 (···), 2.2 V (- - -).

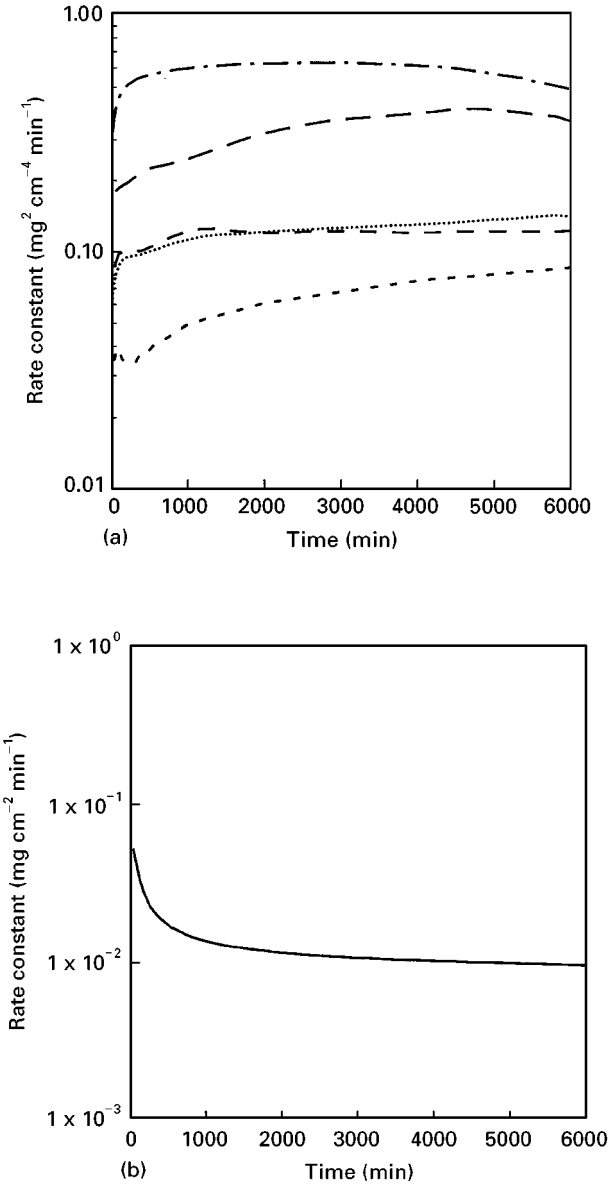

Figure 7 (a) Parabolic oxidation rate constant as a function of time for the binary alloys and the alloys with V, Cr and W oxidized at 815 °C in air. (b) Linear oxidation rate constant as a function of time for the ternary alloys with V and Cr oxidized at 982 °C in air. Ti–48Al plus 1.5Cr (—-—), 600 p.p.m. O_2 (——), 400 p.p.m. O_2 (···), 0.2W (– – –), 2.2V (- - -), 1.4Mn (—).

constants as a function of time while Fig. 7(b) shows the linear rate constants as a function of time for the ternary alloy with Mn. Unlike at 704 and 815 °C, where there was a sharp transient oxidation region followed by a gradual change into a steady state region, at 982 °C the transient region is almost non-existent. The oxidation rate constant reaches its steady state value almost immediately and varies by a factor of almost four for the different alloys. The lowest rate constant is about 6.25×10^{-2} mg^2 cm^{-4} min^{-1} for the ternary alloy with V and about 0.64 mg^2 cm^{-4} min^{-1} for the ternary alloy with Cr. This is shown in Fig. 7. It is important to note that, of all the alloys which exhibited parabolic oxidation the ternary alloy with Cr exhibited the largest weight gain as shown in Fig. 6. In Fig. 7(a) we can see some details from the oxidation data. The ternary alloy with Cr exhibits a small increase in oxidation rate followed by a gradual decline. The initial increase may be attributed to a change in kinetics due to formation of multiple oxides as well as the formation of cracks in the oxide which provide conduits for the passage of oxygen to the metal oxide interface. The subsequent decrease may be attributed to a decrease in the area of the specimen due to the large extent of oxidation. On the other hand the binary alloy with 600 p.p.m. of oxygen exhibits a steady increase in oxidation rate constant with a small decrease at the tail end of the test. This alloy also exhibited severe secondary cracking which explains the increase in the oxidation rate for much of the test. The rest of the alloys exhibited a stable and compact oxide scale which resulted in a steady oxidation rate constant. The mechanism of oxidation of each of the alloys is best studied on a case by case basis.

4.3.1. Ti–48Al Binary Alloys

One alloy with 400 p.p.m. oxygen and the other with 600 p.p.m. oxygen were chosen for the analysis to evaluate if the presence of internal oxygen played a role in the oxidation process. At temperatures of 704 and 815 °C there is no apparent variation in the oxidation behavior, but at 982 °C the alloy with 400 p.p.m. oxygen only gained about 28 mg cm^{-2} after 6000 min while the alloy with 600 p.p.m. oxygen gained as much as 45 mg cm^{-2} after 6000 mins. The apparent differences in the oxidation behaviour can be attributed to the presence of a larger number of cracks and fissures which provide easy paths for the penetration of oxygen. Fig. 8 is a back-scattered electron image of the oxide layers and the base metal in the alloy with 600 p.p.m. of oxygen. There are six distinct regions that can be identified in the photograph. Region **a** is the base alloy. Region **b** is an aluminium depleted (titanium enriched) region close in composition to Ti_3Al at the oxide–metal interface and is approximately

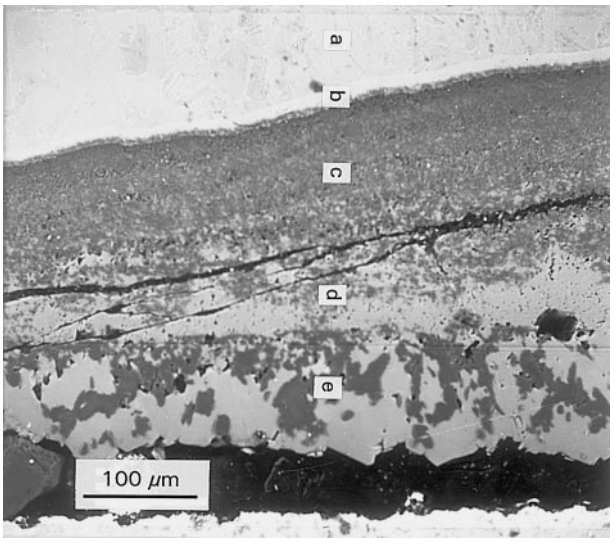

Figure 8 Low magnification back-scattered electron image of the oxide layers and the base metal in Ti–48Al + 600 p.p.m. oxygen oxidized at 982 °C for 6000 min in air. See text for details of each of the regions.

10 μm thick. Region **c** is a compact mixture of aliminium oxide and titanium oxide and is about 120 μm thick. Region **d** contains alternate layers of TiO_2 and Al_2O_3 and is approximately 40 μm thick. Region **e** is continuous TiO_2 with islands of pure Al_2O_3 and is approximately 100 μm thick. The lighter regions correspond to titanium rich oxides while the darker regions are Al_2O_3. There are some large cracks that are present in region **c** which can lead to delamination if the sample is not handled with care. Note that presence of large porosity between layers **d** and **e** as well as within layer **d**. It can be postulated that the rapid outer diffusion of Ti from the lattice to form TiO_2 can leave behind vacancies which can collapse together to form voids by the Kirkendall mechanism. Layer **e** by itself is fully dense with little or no porosity.

The outer oxide layer on the surface was scraped and examined in the transmission electron microscope. A bright field transmission electron micrograph of the powdered oxide is shown in Fig. 9(a). Convergent beam electron diffraction was performed on the largest particle in the micrograph to ascertain its crystal structure. Fig. 9(b) is the selected area diffraction pattern of the region, on comparison with a standard pattern in Fig. 9(c) it is clear that it is a $[1\,1\,\bar{1}]$ zone of TiO_2. This analysis confirms that even though transient oxides may form during the oxidation process, the oxide product in contact with oxidizing medium is always TiO_2.

4.3.2. Ti–48Al–1.5Cr

The ternary alloy with Cr exhibited the worst behaviour of all the alloys that exhibited parabolic oxidation behaviour. Fig. 10 is a low magnification back-scattered electron image of the base alloy and the oxide layers. Five distinct regions are apparent. Region **a** is the base alloy, region **b** is a titanium rich embrittled region about 10 μm thick with a large number of cracks extending inwards from the oxide–metal

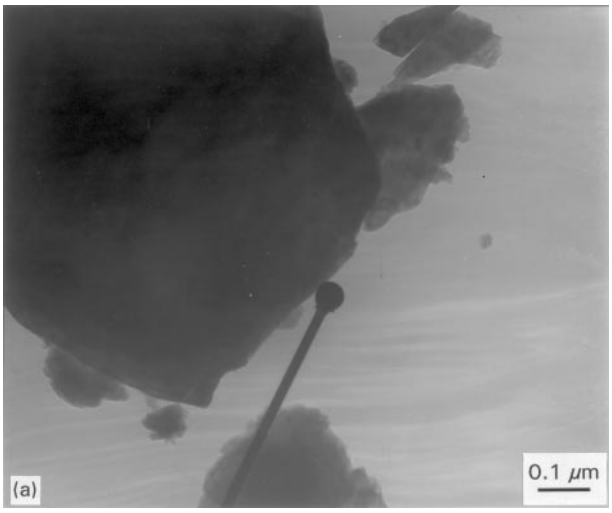

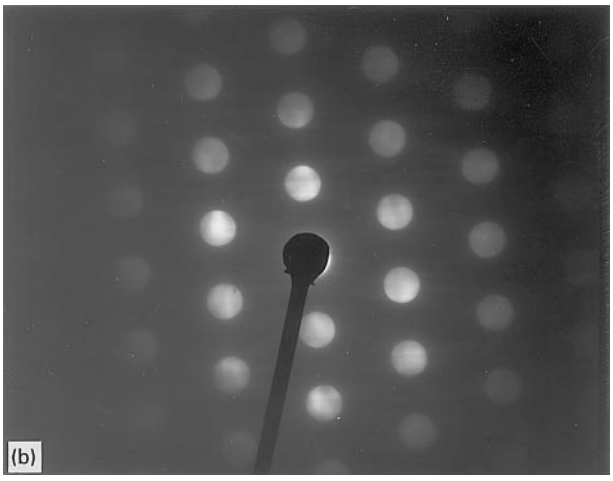

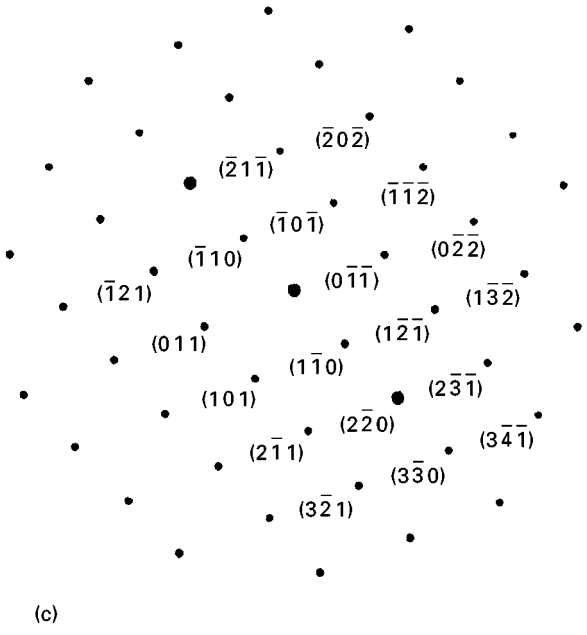

Figure 9 (a) Bright field transmission electron micrograph of the powdered oxide scale on the surface of the Ti–48Al binary alloy oxidized at 982 °C for 6000 min in air. (b) Convergent beam electron diffraction pattern. (c) A computer simulated diffraction pattern showing the $[1\,1\,\bar{1}]$ zone in TiO_2.

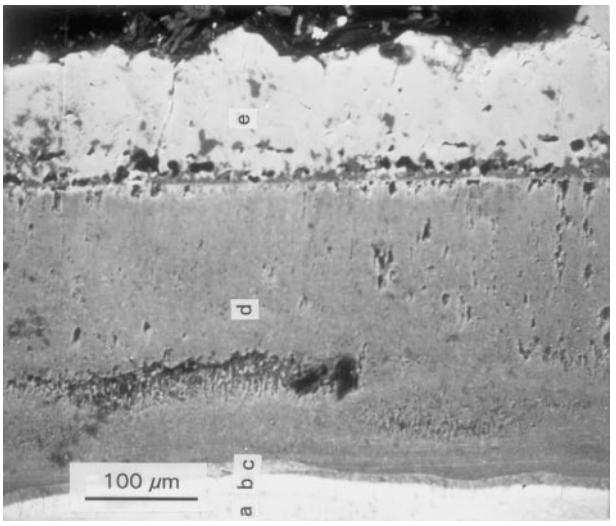

Figure 10 Low magnification back-scattered electron image of the oxide layers and the base metal in Ti–48Al + 1.5Cr. oxidized at 982 °C for 6000 min in air. See text for details of each of the regions.

interface. Region **c** appears to be an oxide layer 10 μm thick which is titanium rich compared to the oxides immediately adjacent to it. Region **d** is a thick Al_2O_3 rich oxide region approximately 250 μm thick which is relatively compact but for some large porosity embedded in it. Region **e** is an outer oxide layer approximately 150 μm thick which is predominantly (> 90 vol %) made up of TiO_2 with very little Al_2O_3 (< 10 vol %) . Fig. 11(a) is a higher magnification back-scattered electron photograph showing regions **a**–**d**. Fig. 11 (b, c) are WDS x-ray dot maps of Ti and Al. It is immediately apparent that region **b** is Ti rich, region **c** has a marginally higher amount of Ti compared to region **d**. An almost continuous layer of porosity exists at the interface between regions **d** and **e**. From this analysis it is apparent that rapid diffusion of Ti to the outside to form the TiO_2 on the outside leaves behind porosity via the Kirkendall mechanism. In addition this depletes region **d** of Ti leading to the formation of an Al_2O_3 rich oxide region. At the oxide–metal interface it is apparent that the inward diffusion of oxygen stabilizes an aluminium depleted region continuous phase which appears to be close in stoichiometry to Ti_3Al. The presence of an aluminium depleted (titanium enriched) region at the metal–oxide interface promotes the formation of an oxide in region **c** which is marginally richer in Ti compared to the surrounding region **d**. The oxygen embrittled region, being very brittle, easily forms cracks. The presence of interconnected porosity in region **d** coupled with the near delamination between regions **d** and **e** provide an easy pathway for the diffusion of oxidation leading to a higher oxidation rate. The addition of Cr, a trivalent element, may also be responsible for the creation of doubly ionized oxygen vacancies, as detailed in the model, which will further worsen the oxidation behaviour. No segregation of Cr was observed at any region of the oxide.

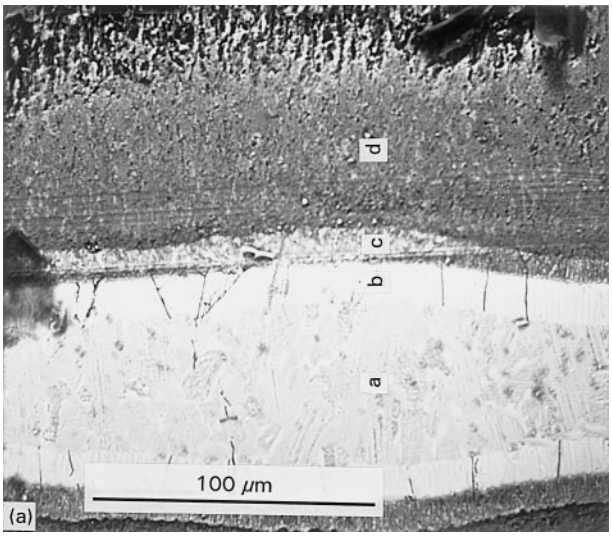

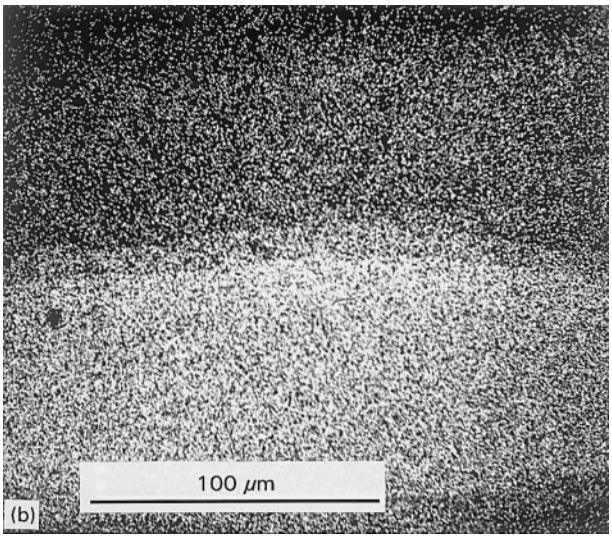

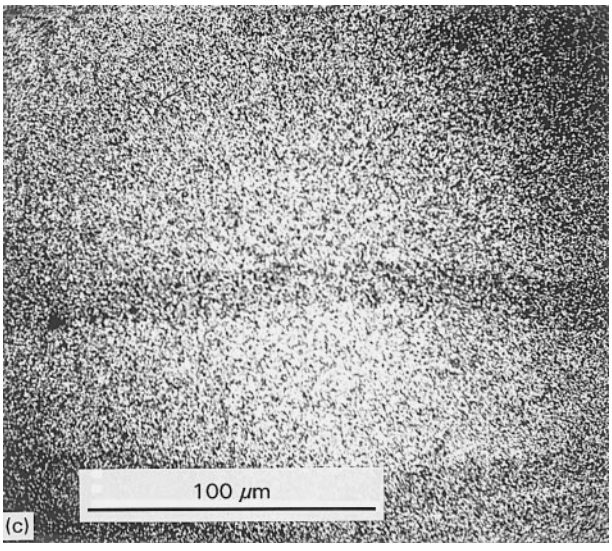

Figure 11 (a) High magnification back-scattered electron image of the oxide layers and the base metal in Ti– 48Al + 1.5Cr. oxidized at 982 °C for 6000 min in air. (b) Ti and (c) Al wavelength dispersive spectroscopy X-ray dot maps.

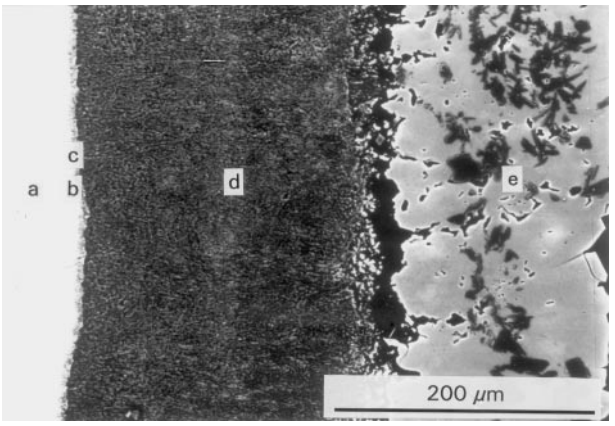

Figure 12 Low magnification back-scattered electron image of the oxide layers and the base metal in Ti– 48Al + 2.2V. oxidized at 982 °C for 6000 min in air. See text for details of each of the regions.

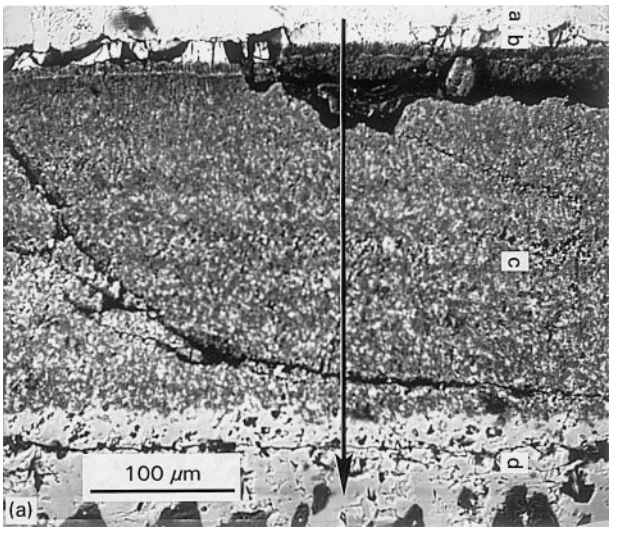

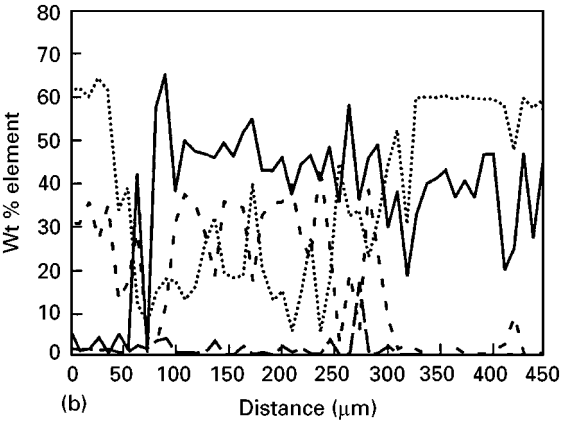

Figure 13 (a) Low magnification back-scattered electron image of the oxide layers and the base metal in Ti–48Al + 1.4Mn. oxidized at 982 °C for 6000 min in air. (b) Compositional line scan using wavelength dispersive spectroscopy for the different elements. —— O; – – – Al; ···· Ti; ——— Mn.

4.3.3. Ti–48Al–2.2V

The ternary alloy with V exhibited the best oxidation resistance of all the alloys oxidized in air at 982 °C. The oxide scale exhibited five distinct regions as in the case of the ternary alloy with Cr. Fig. 12 is a low magnification back-scattered electron image of the various oxide layers. Region **a** is the base alloy as in the other micrographs. Region **b** is a 10 μm oxygen embrittled region just below the oxide–metal interface which appears to be Ti rich and close in composition to Ti_3Al as in the other alloys. However, when compared to the alloy with Cr this region does not have many cracks present in it. Region **c** is about 5 μm thick and is similar to the base alloy and the alloy with Cr. Region **d** is about 200 μm thick and is primarily composed of Al_2O_3. In distinct contrast to the binary alloys and the ternary alloy with Cr where region **d** had extensive amounts of porosity, the corresponding region in the alloy with V has little or no porosity and is a very dense and compact oxide scale. Region **e** is primarily made up of large crystals of TiO_2 (≈70 vol %) with some islands of Al_2O_3 (≈30 vol %) as indicated by the dark regions. The interface between region **d** and **e** is very weak as evidenced by the presence of a large amount of porosity. The outer diffusion of Ti to form TiO_2 may be the reason for the formation of the porosity.

4.3.4. Ti–48Al–1.4Mn

The ternary alloy with Mn exhibited the largest weight gain of all the alloys tested at 982 °C in air with a total weight gain of 58.2 mg cm^{-2} after 6000 min. and exhibited linear oxidation kinetics. The outer oxide scale was very fragile and spalled at a few places when the specimen was being removed from the test setup. The inner oxide scale was adherent. Fig. 13(a) is a low magnification back-scattered electron micrograph of the oxide scale. A line scan was performed from the base metal to the oxide–gas interface of the region highlighted in Fig. 13(a) and is shown in Fig. 13(b). There are four distinct regions. Region **a** is the base alloy, region **b** is a 20 μm thick embrittled layer just below the oxide–metal interface and is rich in titanium. A significant difference in the alloy with Mn is the irregular nature of this region which includes large cracks and a discontinuous appearance. The binary alloys and the alloys with Cr and V had a thin 5 μm oxide layer adjacent to region **b** which was slightly enriched in Ti, this region is absent in this alloy. Immediately next to region **b** is region **c**, which is a large two-phase oxide region about 300 μm thick made up of a dispersion of TiO_2 and Al_2O_3. Fig. 14(a, b, c) are higher magnification back-scattered electron images and corresponding Ti and Al maps of the oxides present in the alloy with Mn. In contrast to the binary alloys and the alloys with Cr and V, this region **c** is made up of a large amount of fine scale porosity which is dispersed evenly throughout the region providing an easy access of oxygen to the inner region. Region **d** is the outermost oxide layer about 100 μm thick in contact with air and is a single phase TiO_2. This layer also contains a large amount of porosity which provides a faster conduit for oxygen to penetrate to the oxide/metal interface.

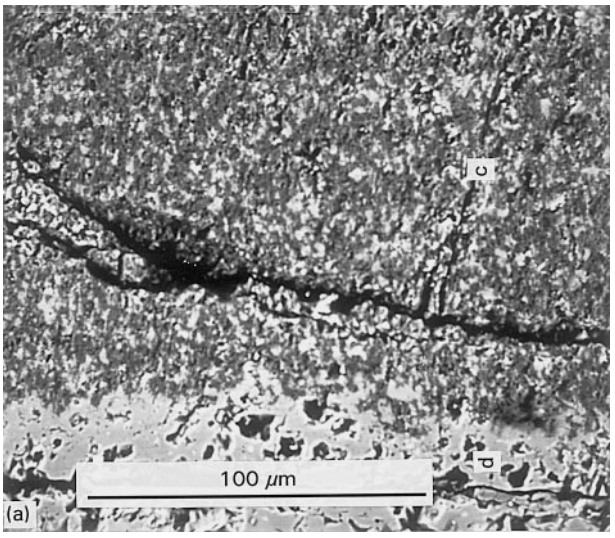

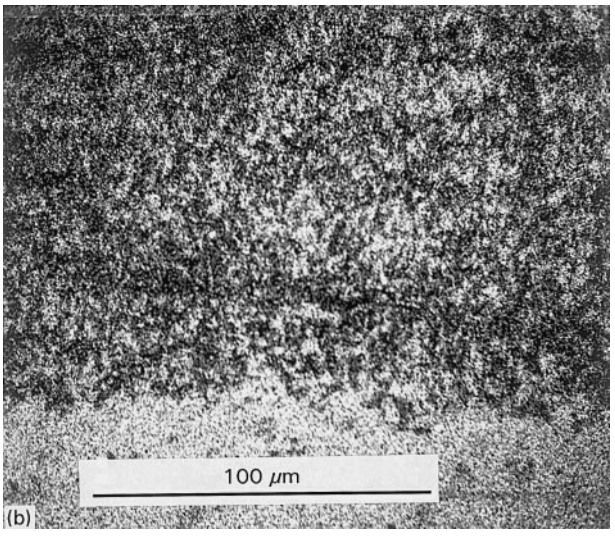

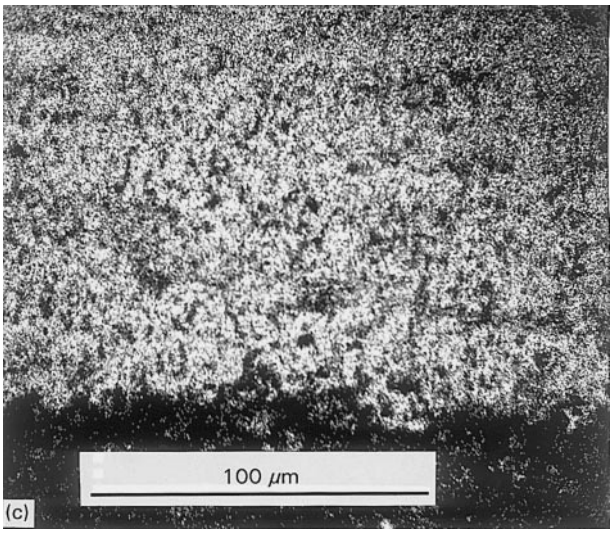

Figure 14 (a) High magnification back-scattered electron image of the oxide layers and the base metal in Ti–48Al + 1.4Mn. oxidized at 982 °C for 6000 min in air. (b) Ti and (c) Al wavelength dispersive spectroscopy X-ray dot maps.

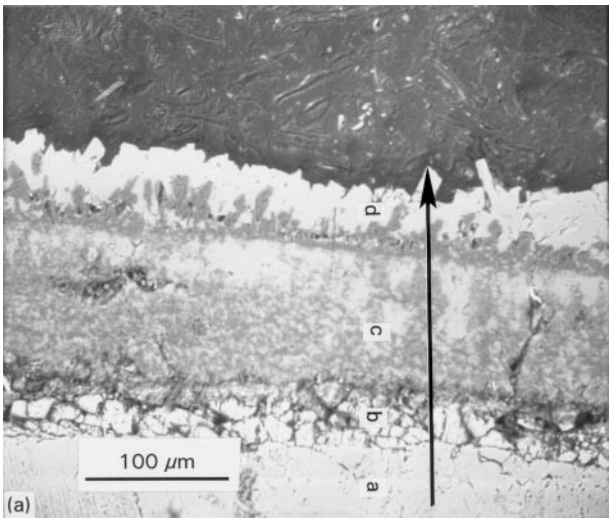

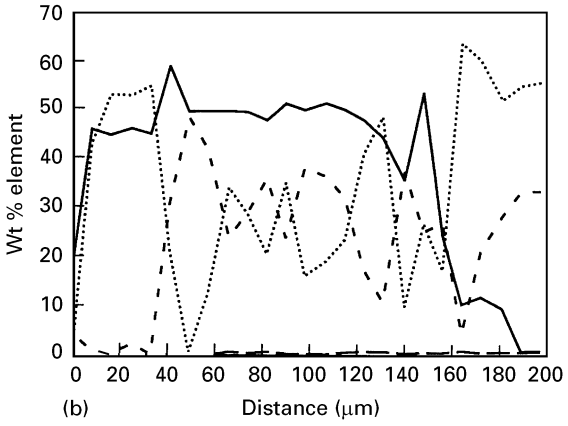

Figure 15 (a) Low magnification back-scattered electron image of the oxide layers and the base metal in Ti–48Al + 0.2W. oxidized at 982 °C for 6000 min in air. (b) Compositional line scan using wavelength dispersive spectroscopy for the different elements. —— O; – – – Al; ···· Ti; ———— W.

4.3.5. Ti–48Al–0.2W

The ternary alloy with W exhibited excellent oxidation response, next only to the alloy with V at 982 °C in air with a total weight gain of 27.16 mg cm^{-2} after 6000 min. The oxide scale had little porosity in it. Fig. 15(a) is a low magnification back-scattered electron image of the oxide layers and Fig. 15(b) is a line scan performed from the base metal to the oxide–gas interface of the region highlighted in Fig. 15(a). There are four distinct regions of interest. Region **a** is the base metal, region **b** is the titanium enriched zone which appears to be embrittled by oxygen. This region is heavily cracked and is rich in oxygen compared to the non-embrittled base metal. Region **c** is about 125 μm thick and is made up of a compact oxide scale with alternating columns of Al_2O_3 and TiO_2. The regions rich in Al_2O_3 can contain TiO_2 dispersed in it while the regions rich in TiO_2 appear to be primarily single phase. Region **d** is about 60 μm thick and has islands of Al_2O_3 protruding into a continuous region of pure TiO_2. Fibres of TiO_2 can be clearly seen protruding out. Fig. 16(a) is a higher magnification back-scattered electron image of regions **c** and **d**. Fig. 16(b, c) are X-ray dot maps of Ti and Al showing clearly the location of the TiO_2 and Al_2O_3. Tungsten

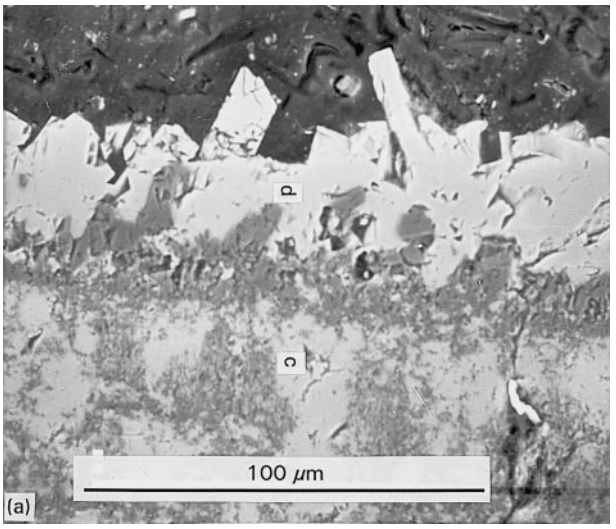

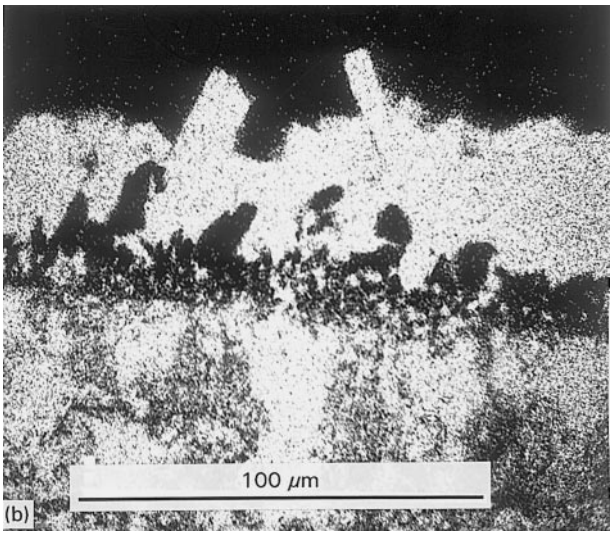

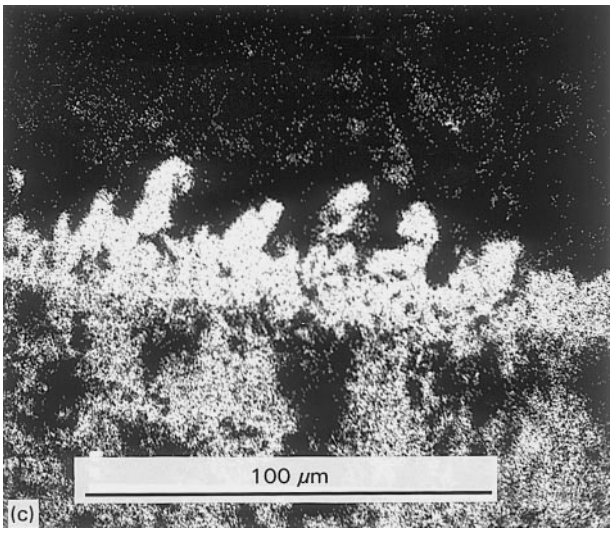

Figure 16 (a) High magnification back-scattered electron image of the oxide layers and the base metal in Ti–48Al + 0.2W. oxidized at 982 °C for 6000 min in air. (b) Ti and (c) Al wavelength dispersive spectroscopy X-ray dot maps.

being a heavy atom is dispersed evenly throughout the oxide, this coupled with a valence of + 6 ties up oxygen vacancies aids in reducing the oxidation rate. In addition the region **d** which has a compact and fully sintered oxide layer without porosity slows down the diffusion of oxygen.

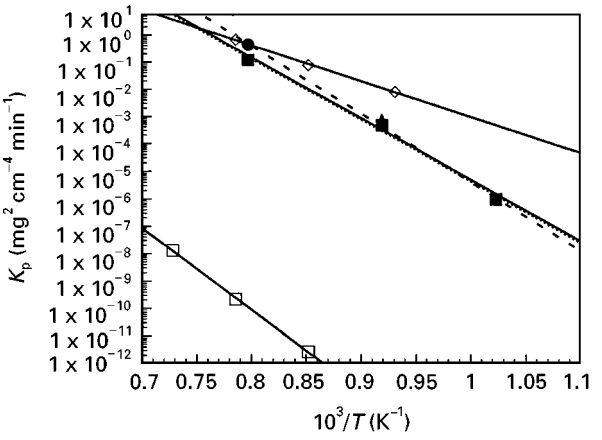

Figure 17 Oxidation rate constants for oxidation in an environment of air plotted as a function of $1000/T$ where T is the temperature of oxidation in K. Superimposed are the kinetics for Al_2O_3 and TiO_2 formation. Ti–48Al + 400 p.p.m. O_2 ■; Ti–48Al + 600 p.p.m. O_2 ●; Ti–48Al + 0.2W ▲; TiO_2 ◇; Al_2O_3 □.

TABLE III Activation energy for oxidation and diffusion

Alloy stoichiometry	Activation energy (kJ mol^{-1})
Ti–48Al (600 p.p.m. oxygen) [this work]	343
Ti–48Al (400 p.p.m. oxygen) [this work]	324
Ti–48Al–0.2 W (at %) [this work]	324
Pure Ti [15]	239
Ti–26Al (at %) [16]	255
Ti–49Al (at %) [16]	419
Ti–50Al (at %) [17]	423
O diffusion in TiO_2 [18]	234
Ti diffusion in TiO_2 [19]	257
O diffusion in Al_2O_3 above 1400 °C [20]	460
O diffusion in Al_2O_3 above 1400 °C [21]	587
O fast diffusion paths in Al_2O_3 [22]	241
Al diffusion in polycrystalline Al_2O_3 [20]	477

4.4. Activation energy for oxidation

The activation energy for alloys that exhibited parabolic oxidation behaviour at all three temperatures of testing were calculated based on the equation

$$K = K_0 \exp(-Q/RT) \quad (16)$$

where K is the oxidation rate constant in mg^2 cm^{-4} min^{-1}, K_0 is a constant with units of mg^2 cm^{-4} min^{-1}, Q is the activation energy in kJ mol^{-1}, R is the gas constant in kJ mol K^{-1} and T is the temperature in K. The ternary alloys with Cr, V and Mn exhibited linear oxidation behaviour at one of the temperatures and the data could not be used for the calculation of activation energies based on this method. Fig. 17 is a plot of ln K as a function of $1/T$. The activation energy data is provided in Table III and varies between 315 to 345 kJ mol^{-1}. It is clear that the presence of different levels of oxygen in the binary Ti–48Al alloy does not play a major role in determining the activation energy. The addition of 0.2 at % W also does not change the activation

energy by much. The activation energy of alloys with higher levels of Al such as Ti–49Al and Ti–50Al (419–423 kJ mol^{-1}) is significantly larger [16, 17]. This may be attributed to the higher aluminium content which promotes the formation of single phase γ phase. The γ phase exhibits significantly better oxidation resistance compared to the α_2-Ti_3Al phase. The activation energy for the oxidation of Ti–48Al base alloys is between the activation energy for diffusion of oxygen in TiO_2 and Al_2O_3.

4.5. Thermodynamic aspects of oxidation

Qualitative and quantitative analyses of the oxide products formed due to oxidation at 982 °C in air for 6000 min were performed. The results indicate two primary oxidation products, Ti-based oxides and Al_2O_3. It is clear from the electron microprobe results that at the oxide–gas interface where the partial pressure of oxygen is the highest, the dominant oxide is TiO_2. Just below this layer of pure TiO_2 are islands of Al_2O_3. In some cases the Al_2O_3 forms a continuous layer and in some cases its exists as discrete islands scattered within the TiO_2. In either case it appears that the formation of TiO_2 selectively removes the Ti from regions adjoining the TiO_2 leading to the enrichment of Al. This coupled with a lower partial pressure of oxygen promotes the formation of large regions of pure Al_2O_3. Below this outer layer is a close packed mixture of oxides made up of Al_2O_3 and Ti-oxides. In this region the partial pressure of oxygen is significantly lower than that found at the oxide–gas interface and hence the formation of either Ti-oxide or Al_2O_3 is driven primarily by composition variations. As detailed in the thermodynamic model, once the Ti oxidizes to form its oxides, the region immediately surrounding it is enriched in Al pushing the alloy into the TiAl + $TiAl_3$ composition range. In this composition range the partial pressure required for the formation of TiO is 3–4 orders of magnitude greater than that required for the formation of Al_2O_3. Thus oxidation proceeds with the formation of alternate particles of Al_2O_3 oxide and Ti-oxide in a compact oxide layer. Just below the metal–oxide interface the alloy is enriched with dissolved oxygen. Oxygen is an α_2-Ti_3Al stabilizer which promotes the formation of a thin 5–10 μm thick aluminium-depleted (titanium-enriched) embrittled region which appears to be close in stoichiometry to α_2-Ti_3Al.

4.6. Kinetics of oxidation

The two major factors that influence the kinetics of oxidation include (i) The diffusion of doubly ionized oxygen vacancies through the oxide layers and (ii) formation of porosity, defects and cracks in the oxide scale.

4.6.1. Diffusion of doubly ionized oxygen vacancies through the oxide

As discussed in the models of oxidation, TiO_2 is a *n*-type semiconductor. The outermost oxide layer is made up of TiO_2 and controls the rate of diffusion of mobile doubly ionized oxygen vacancies in the oxide scale. The alloys with W and V exhibit the best oxidation behavior at 982 °C. V is pentavalent and W is hexavalent. Both these elements can potentially annihilate oxygen vacancies and hence reduce the kinetics of oxidation. On the other hand the presence of Cr leads to poorer oxidation resistance as Cr is a trivalent element promotes the formation of doubly ionized oxygen vacancies and hence increases the kinetics of oxidation at 982 °C. The presence of Mn leads to poorer oxidation resistance and a linear oxidation response at 982 °C. Theoretically Mn being a tetravalent element should not alter the concentration of doubly ionized oxygen vacancies in TiO_2. However, the presence of a large amount of porosity and intergranular cracks appear to promote an easy pathway for oxygen diffusion and a linear oxidation rate.

4.6.2. Intergranular diffusion and formation of defects and cracks in the oxide scale

The presence of easy pathways for oxygen diffusion leads to enhanced kinetics of oxidation. These pathways include intergranular boundaries, interconnected porosity and cracks in the oxide. These factors play a minor role at 704 and 815 °C where the oxide scale is relatively thin but can be significant at 982 °C where oxide scales of the order of 100–200 μm are formed. The binary alloy with 600 p.p.m. oxygen has a higher rate of oxidation compared to the alloy with 400 p.p.m. of oxygen at 982 °C not because of any inherent difference in the mechanism of oxidation, but because the former alloy had interconnected cracks that formed while the latter did not. The two ternary alloys with V and W exhibited the best oxidation resistance in part because they had the most compact oxides with very little porosity. This, coupled with higher valence of the ternary element, lead to a better oxidation resistance. On the other hand, the presence of Mn leads to the formation of a poorly adherent oxide which had extensive amounts of interconnect porosity and cracks which provided easy pathways for the diffusion of oxygen and hence a linear oxidation rate and a large total weight gain at 982 °C.

5. Conclusions

1. The models developed to explain the thermodynamics, kinetics and physical aspects of oxide formation in binary and ternary titanium aluminides appear to fit the experimental results for the oxidation at 982 °C in air with some variations in each case.
2. All the alloys exhibit a parabolic oxidation response at 704 °C with the binary Ti–48Al alloys and the ternary alloy with Mn exhibiting the best oxidation resistance.
3. All alloys except the alloys with Cr and V exhibit a parabolic oxidation behaviour at 815 °C. The alloys with Cr and V exhibit a linear oxidation behaviour.

4. At 982 °C all the alloys except the alloy with Mn exhibit a parabolic oxidation behaviour. The ternary alloy with Mn exhibits a linear oxidation behaviour.
5. The alloys with V and W exhibit the best oxidation behaviour at 982 °C indicating that they may be tying up the doubly ionized oxygen vacancies required for transport of oxygen. In addition the formation of a compact scale reduces easy pathways for the diffusion of oxygen.
6. The addition of Cr, a trivalent element, is detrimental to the oxidation behaviour at all temperatures. The presence of Cr^{3+} ions can promote the formation of doubly ionized oxygen vacancies and increases the rate of oxidation.
7. The outermost oxide layer in contact with air at 982 °C is stoichiometric TiO_2 in all the alloys.
8. In the overall context the addition of the small amounts of ternary elements does not lead to much changes in the oxidation behaviour. Any further investigation in this area must focus on larger additions of ternary elements.

Acknowledgements

Experimental assistance provided by Mr Douglas Shelton and Mr James Toney is gratefully acknowledged. The authors wish to thank Dr Soboyejo for providing the samples. This research was partly supported by the Materials Science and Engineering Program at The University of Texas at Arlington.

References

1. E. L. HALL and S. C. HUANG, "High temperature ordered intermetallic alloys III", edited by C. T. Liu, A. I. Taub, N. S. Stoloff and C. C. Koch (Pittsburgh, PA, Materials Research Society, 1989) p. 373.
2. S. C. HUANG and E. L. HALL, *Metall. Trans. A* **22** (1991) 2619.
3. Y. W. KIM, *J. Metals* **41** (1989) 24.
4. C. WAGNER, *Atom Movements*, ASM **C** (1951) 153.
5. S. TANIGUCHI, T. SHIBATA and S. ITOH, *Mater. Trans.* **32** (1991) 156.
6. A. RAHMEL and P. J. SPENCER, *Oxidation of Metals* **35** (1991) 53.
7. D. R. GASKELL, "Introduction to Metallurgical thermodynamics", (McGraw-Hill-Kogakusha Ltd., 1973) p. 269.
8. Y. T. PENG, P. B. ASWATH and A. R. KOYMEN, *Met. Trans. A* **25** (1994) 1041.
9. P. KOFSTAD, "High temperature corrosion" (Elsevier Applied Science Publishers Ltd., New York, NY, 1988) p. 244.
10. P. KOFSTAD, P. B. ANDERSON and O. J. KRUDTAA, *J. Less Common Metals* **3** (1961) 89.
11. K. HAUFFE, "Oxidation of metals" (Plenum Press, 1965) p. 217.
12. P. KOFSTAD, "Nonstoichiometry, diffusion and electrical conductivity in binary metal oxides" (John Wiley and Sons Inc., 1972) p. 15.
13. S. N. SANKARAN, R. L. CLARK, J. UNNAM and K. E. WIEDEMANN, Nasa Technical Paper, (1990) 3012.
14. R. A. PERKINS, K. T. CHIANG, G. H. MEIER and R. MILLER, in "Oxidation of high temperature intermetallics", edited by T. Grobstein and J. Doychak (The Minerals, Metals and Materials Society, 1989) p. 157.
15. A. M. CHAZE, C. CODDET and G. BERANGER, *J. Less Common Metals.* **83** (1982) 49.
16. G. WELSCH and A. I. KAHVECI, in "Oxidation of high temperature intermetallics", edited by T. Grobstein and J. Doychak (The Minerals, Metals and Materials Society, 1989) p. 207.
17. N. S. CHOUDHURY, H. C. GRAHAM and J. W. HINZE, in Proceedings of Symposium on Properties of High Temperature Alloys, edited by Z. A. Foroulis and F. S. Pettit, Electro-Chemical Society Proceedings **77–1** (1976) 668.
18. J. UNNAM, R. N. SHENOY and R. K. CLARK, *Oxidation of Metals* **26** (1986) 231.
19. D. L. VENKATU and L. E. POTEAT, *Mat. Sci. Eng.* **5** (1969/1970) 258.
20. Y. OISHI and W. D. KINGERY, *J. Chem. Phys.* **33** (1960) 905.
21. K. P. D. LANGERLOF, T. E. MITCHELL and A. H. HEUR, in "Solute-defect interaction", edited by S. Saimoto, G. R. Purdy and G. V. Kidson (Pergamon Press, 1986) 152.
22. High Temperature Oxidation-Resistant Coating, Committee on Coatings, National Materials Advisory Board, National Academy of Sciences, (1970) 29.

Received 12 October 1994
and accepted 9 November 1995